Microstructural Evolution and Mechanical Properties of Constrained Groove-Pressed 304 Austenitic Stainless Steel

Rahul Singh, Deepak Singh, Deepak Sachan, Surya Deo Yadav, and Abhishek Kumar ⓘ

The present work investigates the influence of constrained groove pressing (CGP) on the microstructural evolution and mechanical properties of 304 austenitic stainless steel. CGP shows a significant improvement in mechanical properties such as tensile strength and micro-hardness. XRD analysis shows the transformation of austenite phase into deformation-induced martensite phase which is also confirmed by vibrating sample magnetometer. Finite element analysis employing Deform 3D software shows the average induced strain of 2.29, after two passes of CGP. Rietveld refinements on XRD patterns affirm the decrease in crystallite size, increase in microstrain and dislocation density. EBSD also shows the formation of substructures due to CGP. The ultimate tensile strength of solution-treated specimens enhances from 729 to 1058 MPa, and the value of micro-hardness increases from 238 to 477 VHN after two passes of CGP. The augmentation in mechanical properties is attributed to the synergic effect of increased dislocation density, martensitic transformation, substructure formation and reduced crystallite size.

1. Introduction

Presently, stainless steels are used in different industrial sector for a variety of applications. Because of their growing need in different sectors, there is need of steels with superior mechanical properties. Austenitic stainless steels (ASS) are extensively used in various applications such as power plants, petroleum and chemical industries; because of their high corrosion resistance, high thermal stability and excellent weldability (Ref 1). The steels are limitedly used in structural application because of their lower strength (Ref 2). These steels can be made suitable for structural application by improving mechanical properties, which can be achieved by different strengthening mechanisms such as reduction in grain size and strain hardening. Among various strengthening methods, grain refinement is a suitable and reliable way to enhance the strength (Ref 3). Severe plastic deformation (SPD) is defined as metal forming/working technique which involves very large strains. Various SPD techniques were developed and proposed in order to obtain fine-grained materials, over the past couple of decades (Ref 4). The CGP based on severe plastic deformation (SPD) is efficient to yield fine grains in metallic materials and thereby

enhances mechanical properties (Ref 5). During SPD, dislocation density increases and dense dislocation walls are formed. The dislocations and dislocation walls impede the motion of mobile dislocations and hence strengthen the metallic materials.

CGP has been successfully implemented on pure Al (Ref 6–9), Al AA3003 alloy (Ref 10), pure copper (Ref 11), pure Ni (Ref 12), Al–Mg alloy (Ref 13), brass (Ref 14, 15), low carbon steels (Ref 16, 17), HSLA automotive steel (Ref 18) and IF steel (Ref 19). CGP resulted in the formation of micrometer-sized subgrains with well-defined grain boundaries and has shown superior mechanical properties in comparison with other SPD processes. The processing temperature during CGP of pure Al has significantly influenced the grain refinement of microstructure (Ref 7). The banded subgrains in pure Al have formed due to the significant refinement of microstructure in the shear regions (Ref 8). Tensile and yield strengths improved with the loss in ductility as the CGP progresses. An experimental study on the influence of CGP parameters such as strain rate and number of passes on grain size, hardness and tensile properties showed that the number of passes was the most significant parameter followed by strain rate (Ref 9). CGP on AA3003 Al alloy showed the improvement in mechanical properties and after three passes, the grain size was reduced to 580 nm with an improvement in yield and tensile strength (Ref 10). The effect of stress relief annealing on CGPed pure copper showed that the mechanical properties and homogeneity increase with the decrease in mean grain size. With subsequent passes, the mechanical properties decreased due to increased microstructure heterogeneity (Ref 11). CGP of pure nickel resulted in a significant rise in yield and tensile strength after the first pass, whereas a marginal drop was witnessed after the third pass due to increased dislocation recovery at higher strains (Ref 12). CGPed Al-Mg alloy showed grain refinement with significant improvement in hardness, yield and tensile strengths ($\sim$ 55%, 110% and 20%, respectively), with a considerable loss of elongation ($> 90\%$) in the first two passes along with thermo-mechanical treatment (Ref 13). CGP of brass resulted in

Rahul Singh, Deepak Singh, Deepak Sachan, and **Abhishek Kumar**, Department of Applied Mechanics, Motilal Nehru National Institute of Technology Allahabad, Prayagraj 211004, India; and **Surya Deo Yadav**, Department of Metallurgical Engineering, Indian Institute of Technology BHU, Varanasi 221005, India. Contact e-mail: abhishek@mnnit.ac.in.
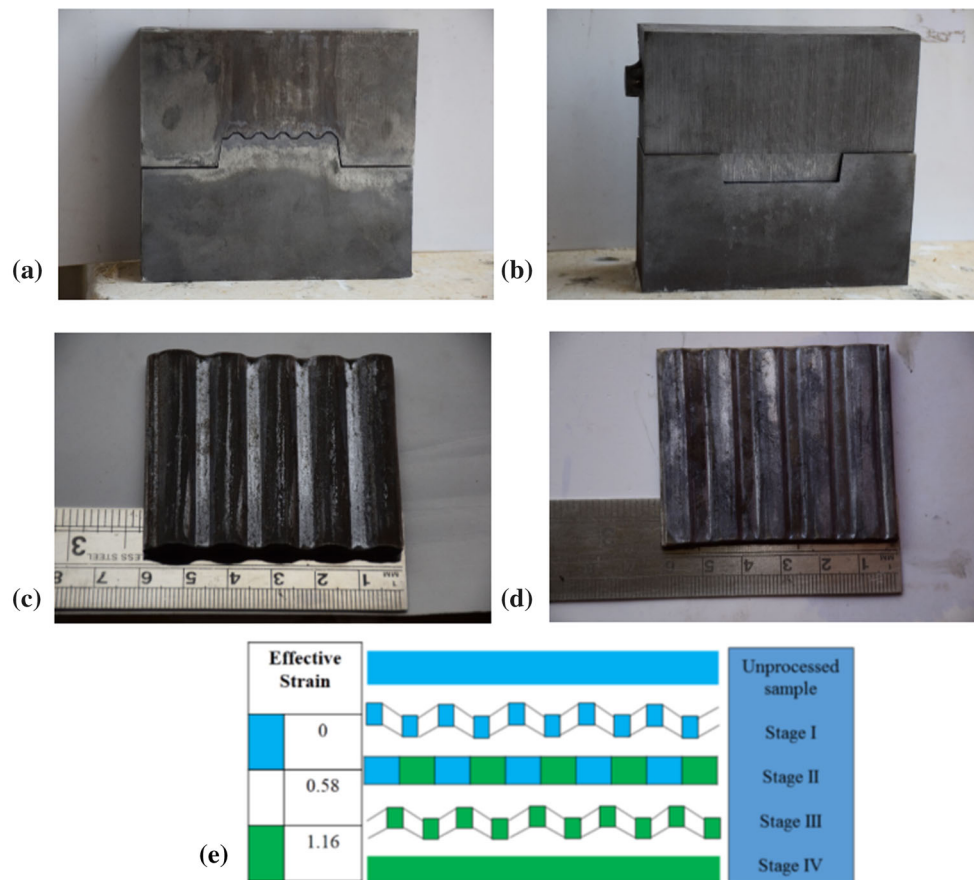
Fig. 1 Grooving dies (a), flattening dies (b), specimen after first grooving (c), final specimen after pass 1 (d), and effective Von Mises strain induced in the specimen during various stages of a single pass of CGP (e)

the improvement in wear resistance (Ref 14) and non-uniform distribution of equivalent strain which in turn results in non-uniformity in microstructure and hardness (Ref 15). A high magnitude of strain, i.e., 4.64 was induced in the low carbon steel through CGP, which resulted in grain size of 230 nm and ultimate tensile strength of 400 MPa (Ref 16). Kumar et al. (Ref 17) employed CGP over low carbon steel and reported the improvement in strength from 300 to 576 MPa with the drop in ductility from 40% to 7.5% after 4 passes of CGP. Karademir et al. (Ref 18) employed CGP over S400MC HSLA steel and reported the improvement in yield and tensile strength to 677 and 714 MPa, respectively, with an improvement in hardness value from 248 to 265 HV after 4 passes of CGP. Shahraki et al. (Ref 19) studied the effect of CGP over mechanical properties of IF steel and reported grain refinement from 45 to 243 nm after four passes. They observed the increase in tensile strength up to the second pass and thereafter, decrease in tensile strength. The FE analysis of CGPed copper sheet showed accurate results and predicted distribution of hardness was more homogeneous with larger strain with good agreement to the experimental results (Ref 20). Nazari et al. (Ref 21) investigated deformation behavior of pure copper processed through CGP, both analytically and experimentally. The complete process of CGP was divided in bending, stretching and pressing sections. It was found that the stretching section is more effective to obtain good combination of high ultimate strength and good formability. Khodabakhshi et al. (Ref 22)

studied CGP-cross route using 3D FE analysis and validated the experimental results for low carbon steel.

A lot of research has been carried out in the last decades on CGP on a variety of materials, but there is no work reported on the deformation behavior of 304 ASS employing CGP. Therefore, in the present work, an effort has been made to study the microstructural evolution and to investigate the mechanical properties such as hardness, ultimate tensile strength and toughness of 304 ASS. A comprehensive study using FE analysis has also been carried out to understand the influence of CGP on the strain distribution of 304 ASS employing DEFORM 3D.

2. Simulation and Experimentation

Commercially available 304 ASS was procured in form of sheet (1 m × 1 m) of thickness 3 mm. Specimens of dimensions 60 mm × 50 mm × 3 mm were machined and solution-treated (homogenized at 1050 °C for 1 h) for further CGP. The chemical composition of procured sheet material was analyzed using optical emission spectroscopy (OES), and detected alloying elements (in weight %) are 18.2 Cr, 8.59 Ni, 0.068 C, 0.003 S, 0.070 P, 0.408 Si, 1.24 Mn and balance Fe. An asymmetrical die fabricated from D2 steel having 45º groove angle and 3 mm groove width was employed for repetitive shear deformation of 304 ASS. Figure 1 shows the CGP dies
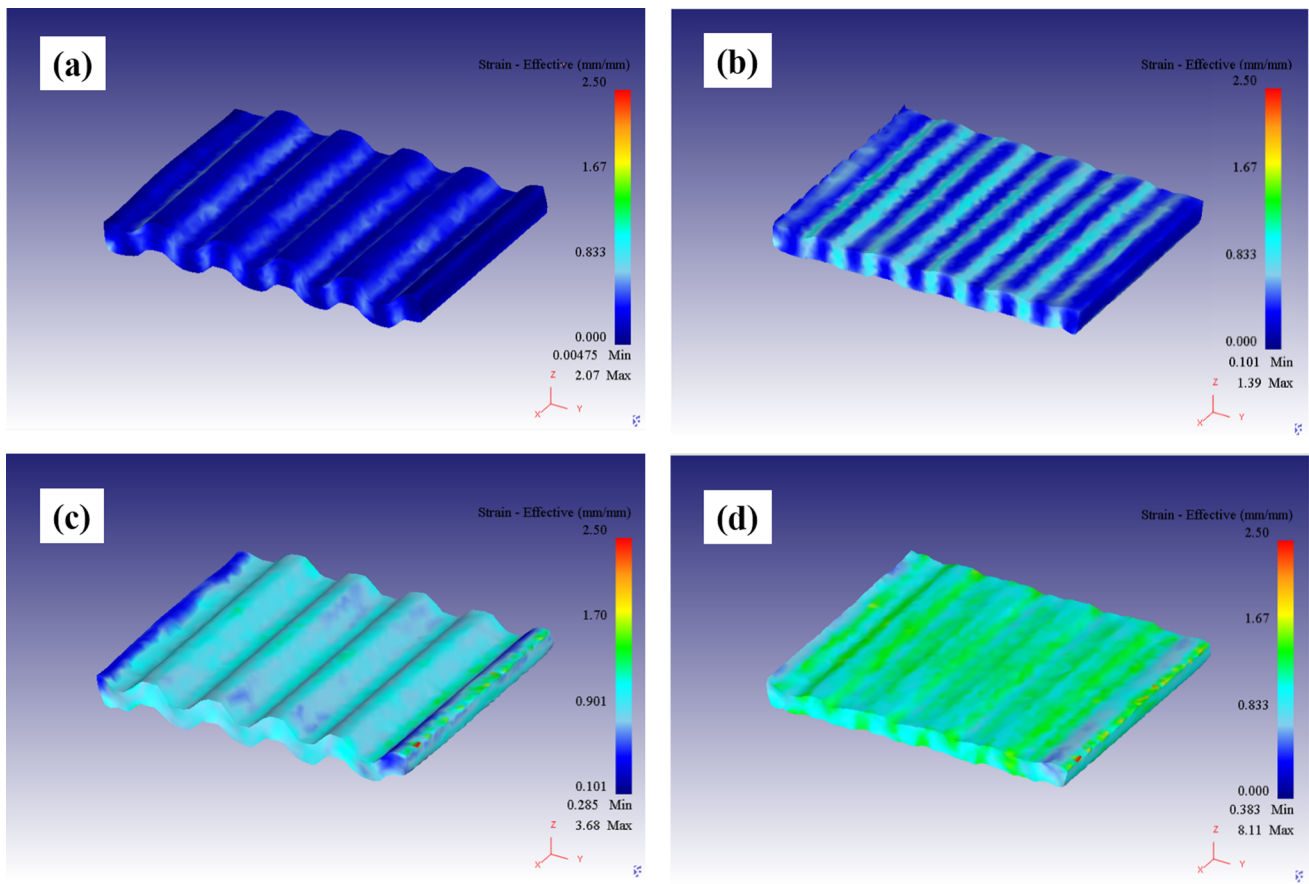
Fig. 2 Effective plastic strain contours obtained by FE simulation during the first pass. First grooving (stage I) (a), First flattening (stage II) (b), Second grooving of the specimen after 180º rotation (stage III) (c), and Second flattening of the specimen (stage IV) (d)

used for deformation and processed specimens at different stages of the first pass. The die shown in Fig. 1(a) was used for grooving, and the die shown in Fig. 1(b) was utilized for straightening the samples after every step of grooving. Figure 1(c) depicts the deformed zigzag sample as a result of first grooving. A single pass of CGP consists of four stages viz. grooving followed by flattening and then with one 180° rotation of specimen and again steps of grooving and flattening. After completion of one pass, an effective equivalent strain of 1.16 is induced uniformly throughout the specimen (Ref 6). Figure 1(d) depicts the final shape of the specimen after completion of the first pass. The effective Von Mises strain encountered in each stage of one complete pass of CGP processing is schematically illustrated in Fig. 1(e). Specimens were CGPed (up to 2 passes) at room temperature employing a hydraulic press of 200 ton capacity with a persistent pressing speed of 0.1 mm/s. Molybdenum disulfide (MoS₂) was used as a lubricant between the samples and processing dies to reduce friction during deformation.

Numerical analysis was carried out employing software DEFORM-3D to understand the hardening behavior of 304 ASS processed by CGP. The actual size of the specimen and the die was modeled for simulating the real experiment. The dies were considered as a rigid.

The material properties were taken from the library of DEFORM-3D as AISI 304 ASS to simulate the CGP process. The power law was used in the present to follow the true behavior of steel. Simulations were carried out with 50,000

tetrahedral elements. At the sample and die interface, a constant shear friction of value $m = 0.12$ was used (Ref 23). Automatic re-meshing technique was utilized to take care of the large strains, and direct iteration solver method was applied. The optimum element size was obtained as 0.584 mm by comparing the strain values of FE analysis with Von Mises strain.

XRD studies were performed employing Rigaku Smartlab diffractometer having Cu-K$_\alpha$ radiation. XRD analyses were carried out for specimens in solution-treated and CGPed state to investigate the phase transformations in 304 ASS. Rietveld analysis was performed on the XRD patterns of solution-treated and CGP processed samples employing MAUD software to evaluate microstrain and crystallite size. The assurance of refinement quality was decided on the basis of R_w and R_{wnb} (without background) values (Ref 24). Light optical microscopy (LOM) using Leica 5000 M was employed for taking the micrographs. In order to estimate the amount of α'-martensite in processed steel, experiments were also conducted on vibrating sample magnetometer (VSM) in an applied magnetic field of 1 Tesla. EBSD measurements were conducted on samples of size 10 mm × 10 mm. The specimens were first mechanically polished up to 2000 grit size followed by wet cloth polishing over double dish polishing machine using alumina powder. Afterward, electro-polishing was done to achieve excellent strain-free surfaces using methanol and perchloric acid in a ratio of 80:20 at 18 volts for 18 s. An FEI-Nova machine was used to perform the EBSD measurements. The obtained data from EBSD measurements were analyzed using TSL OIM
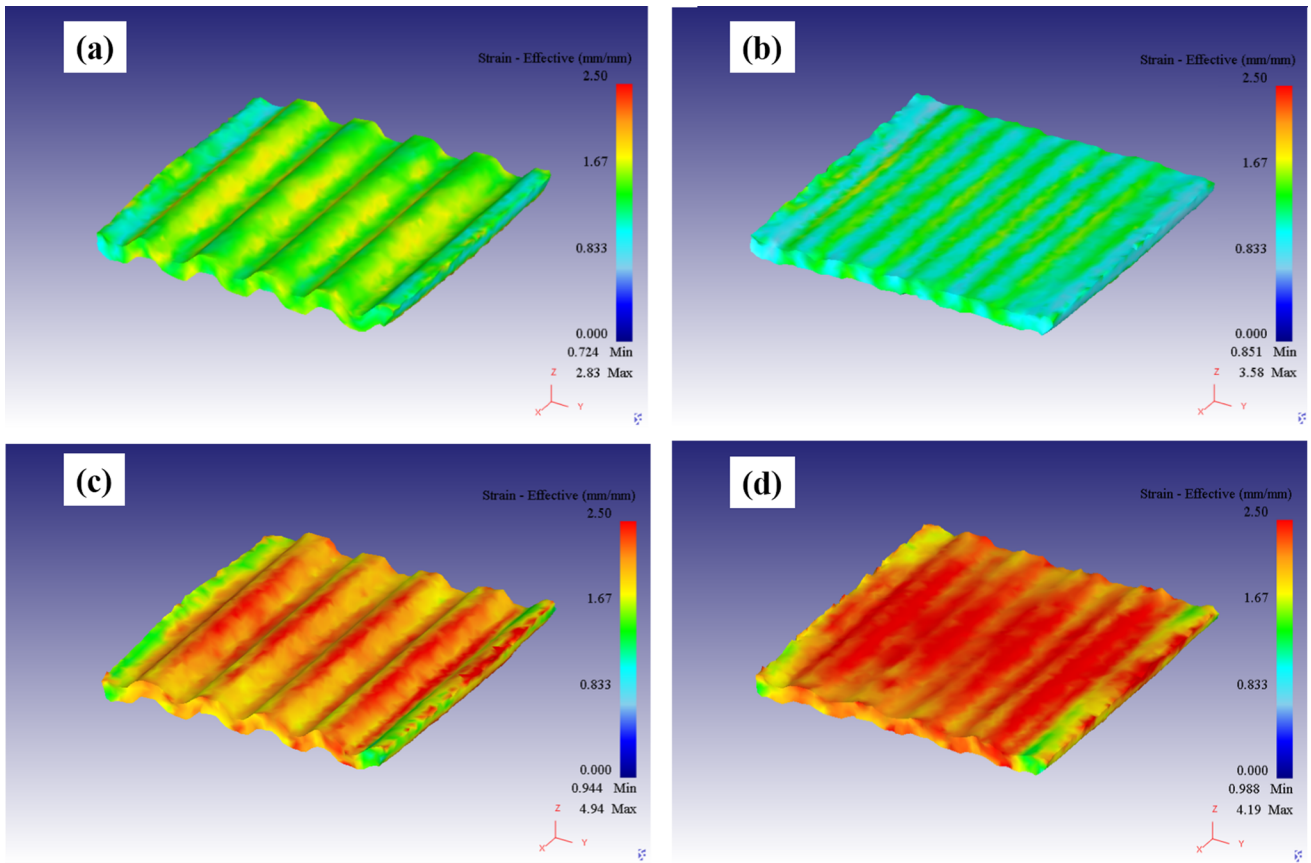
Fig. 3 Effective plastic strain contours obtaind by FE simulation during second pass. (a) First grooving (stage I), (b) First flattening (stage II), (c) Second grooving after 180º rotation (stage III), and (d) Second flattening (stage IV)
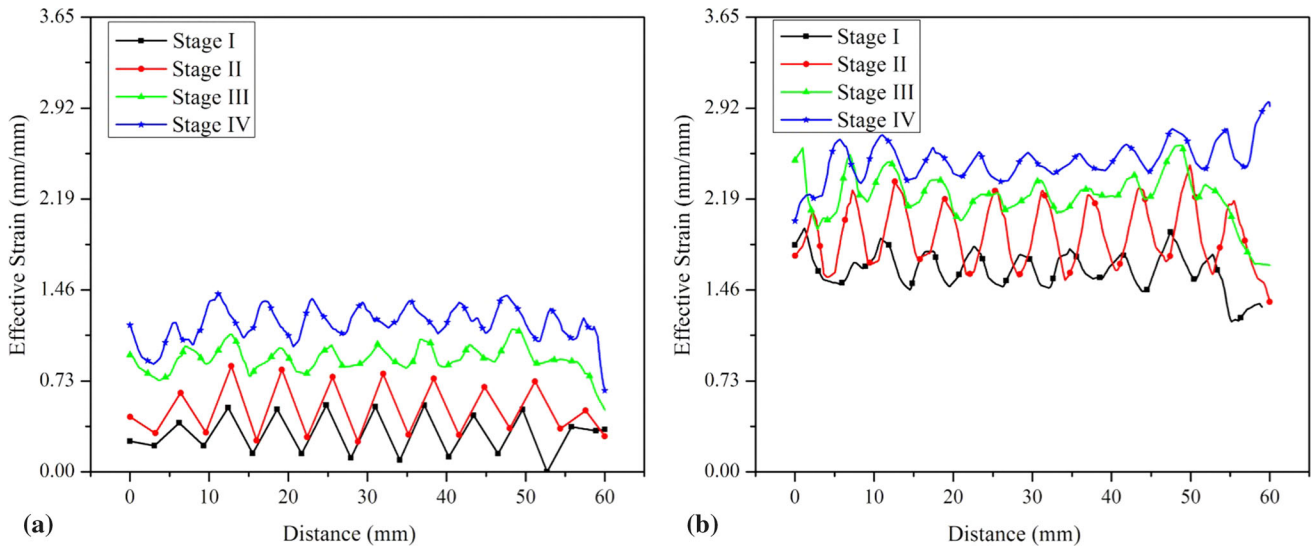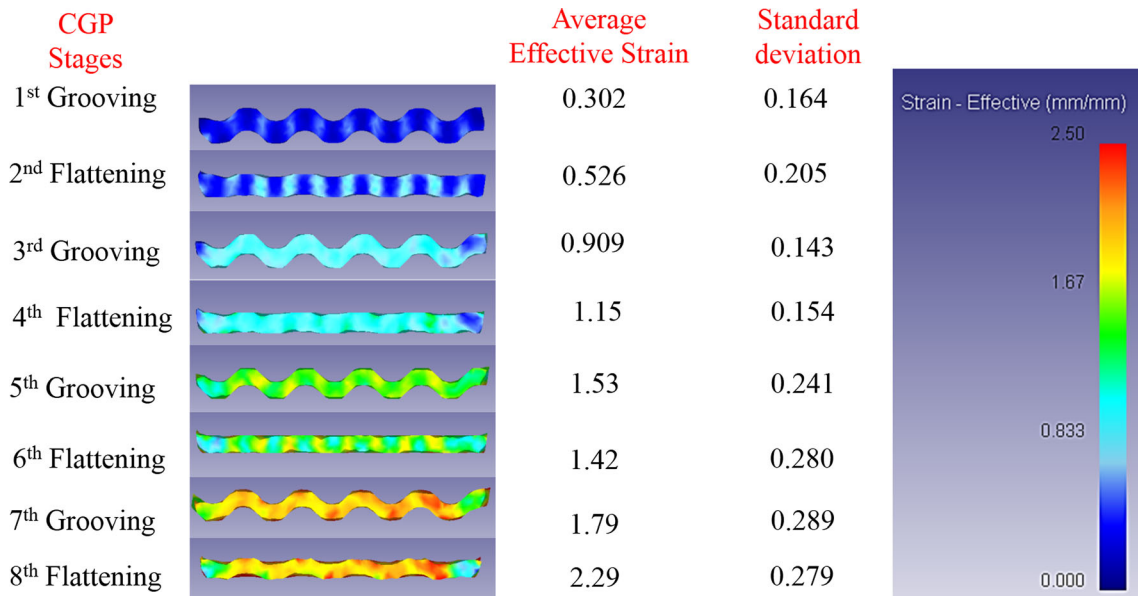

Fig. 4 Distributions of effective strain in mid-section of the specimen after first pass (a) and second pass (b)
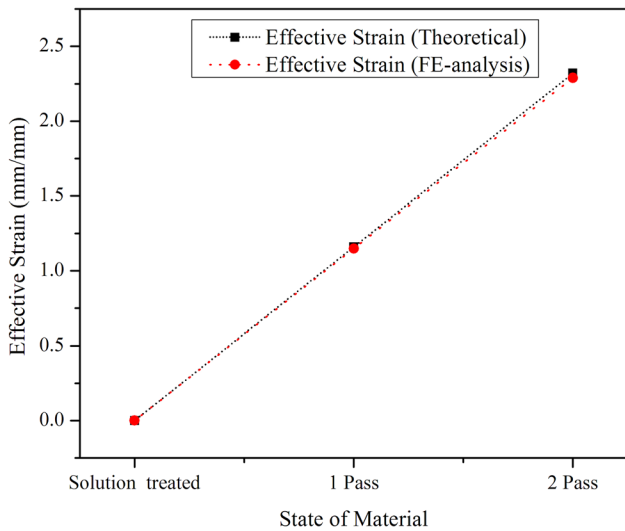
EBSD analysis software to understand the sub-structural evolution. The amount of local plastic deformation can be quantified with the help of kernel average misorientation (KAM) map, which is average misorientation angle of a given point with respect to all neighbors. Misorientation less than 5° is considered in the study of KAM. Blue color in KAM map corresponds to lower strain due to a low degree of misorientation. Increase in region of green in KAM maps indicates the increase in strain with the increase in CGP passes. Some dark regions visible in KAM maps represent un-indexed highly strained areas.

| CGP Stages		Average Effective Strain	Standard deviation
1st Grooving		0.302	0.164
2nd Flattening		0.526	0.205
3rd Grooving		0.909	0.143
4th Flattening		1.15	0.154
5th Grooving		1.53	0.241
6th Flattening		1.42	0.280
7th Grooving		1.79	0.289
8th Flattening		2.29	0.279

Fig. 5 Evolution of plastic strain in 304 ASS specimens at different stages of the CGP process

Fig. 6 Comparison of effective plastic strain obtained by theoretical and FE analysis
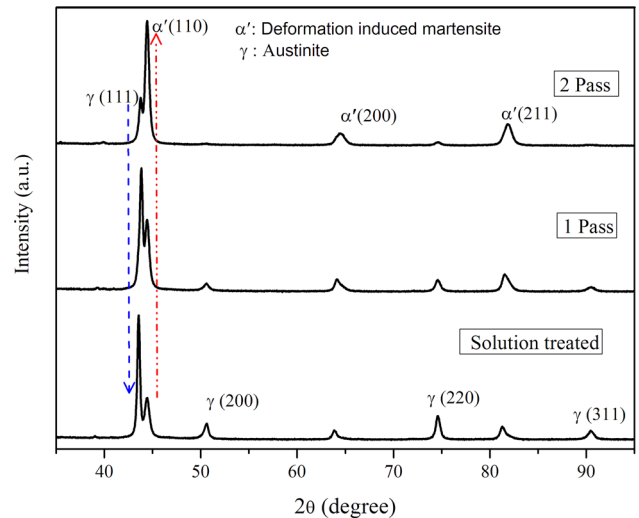
**Fig. 7** Indexed XRD patterns of solution-treated and CGPed specimens

The mechanical response of solution-treated and CGPed 304 ASS specimens was studied through tensile and hardness tests. Sub-size tensile specimens of gauge length of 16 mm, width of 4 mm and thickness of 2 mm were fabricated in accordance with ASTM E8 standard. Tensile tests were performed at environmental conditions employing a BISS 25 kN tensometer. Five samples of each condition were tested to investigate the reliability of results. Toughness was calculated as the area under the engineering stress strain curves. Hardness testing was performed at ambient conditions using UHL-VMHT micro-hardness tester at different locations of the specimen's surface employing a load of 500 gmf and a dwell time of 15 s. Average hardness values were evaluated from at least 20 measurements of each condition. Prior to hardness tests, the samples were mechanically polished using emery papers of grit size ranging

from 320 to 2000. Subsequently, cloth polishing over double dish polishing machine using alumina particles of size 0.05 μm was employed to get a mirror-like surface.

3. Results and Discussion

3.1 Finite Element Analysis

During CGP, the austenitic stainless steel undergoes severe deformation and the amount of strain induced is huge within specimens. As per theoretical analysis of CGP, the strain induced is homogeneous throughout the processed specimen (Ref 5). The analysis of CGP deformation assumes simple shear
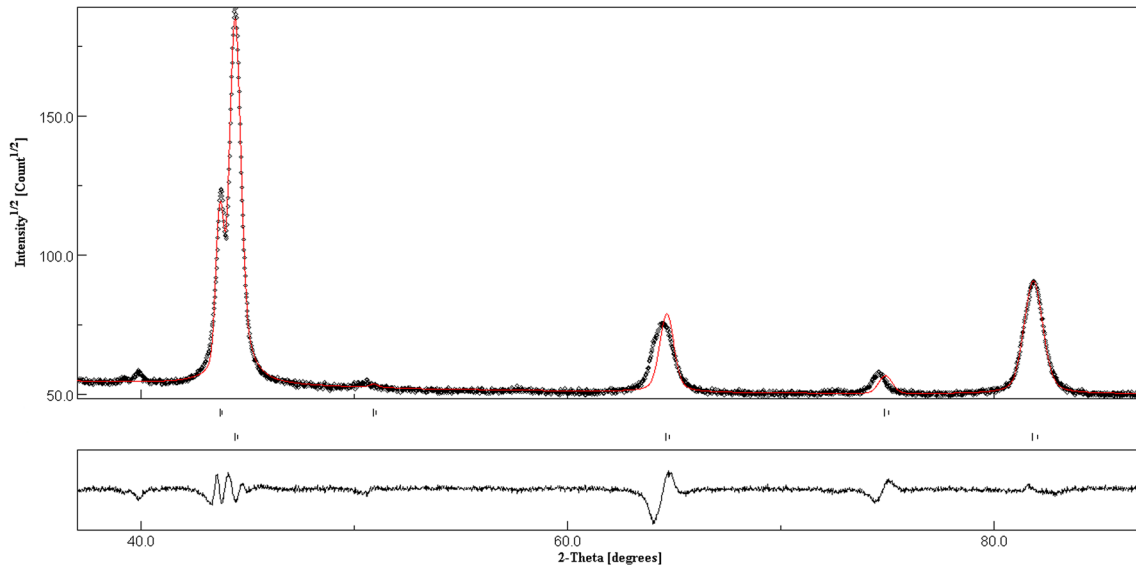
Fig. 8 Rietveld plot after second pass showing the experimental data as points and refinement data as a continuous line. The bottom plot indicates the residuals

Table 1 Crystallite size, microstrain, average internal dislocation density, and quality factors obtained from Rietveld analysis

S. no	Sample	Crystallite size, nm		Microstrain		Dislocation density, m^{-2}		R_w, %	R_{wnb}, %
		γ	α'	γ	α'	γ	α'		
1	Solution treated	395.87	100.68	...	4.12×10^{-3}	...	9.37×10^{14}	6.06	1.80
2	1 Pass CGPed	206.00	89.00	3.52×10^{-3}	4.99×10^{-3}	4.75×10^{14}	1.28×10^{15}	7.52	1.78
2	2 Pass CGPed	125.40	69.41	3.64×10^{-3}	5.55×10^{-3}	8.08×10^{14}	1.83×10^{15}	4.83	1.73

condition. The imposed Von Mises strain (ε) induced within the specimen may be calculated by using Eq. 1

$$\varepsilon = \frac{\sqrt{2}}{3} \left\{ \left(\varepsilon_x - \varepsilon_y\right)^2 + \left(\varepsilon_y - \varepsilon_z\right)^2 + \left(\varepsilon_z - \varepsilon_x\right)^2 \right. \\ \left. + 6\left[\left(\varepsilon_{xy}\right)^2 + \left(\varepsilon_{yz}\right)^2 + \left(\varepsilon_{zx}\right)^2\right] \right\}^{1/2} \quad \text{(Eq 1)}$$

where, ε_x ε_y and ε_z are normal strains, and ε_{xy}, ε_{yz} and ε_{zx} represent shear strain. The die used for grooving is designed with groove angle 45° for sample thickness of 3 mm in such way that single pressing induces shear strain of value 1 in the deformed zone. This shear strain γ follows from the geometry by inserting the groove angle $\theta = 45°$, the width of shearing $t = 3$ mm and the shearing distance $\Delta x = 3$ mm into Eq. 2.

$$\gamma_{xy} = \Delta x/t = \tan 45° = 1 \quad \text{(Eq 2)}$$

Now, invoking shear strain condition $\varepsilon_{xy} = \gamma_{xy}/2$ and with the assumption that there is no expansion in longitudinal and transverse direction, i.e., $\varepsilon_x = \varepsilon_y = \varepsilon_z = \varepsilon_{yz} = \varepsilon_{zx} = 0$, Eq. 1 leads to an effective strain of 0.58 in first step of grooving. In this way, strain magnitude of 1.16 and 2.32 is induced in the specimens after first and second pass of CGP, respectively, as shown in Fig. 1(e) which reflects the various stages of one pass and the effective strain incorporated within the deformed and un-deformed regions. Yoon et al. (Ref 25) reported that the

deformation mode during analytical evaluation of strain is considered to be simple shear, which may enhance or decrease the magnitude of the imposed strain. Figure 2 and 3 shows the results of Deform 3D simulation and depicts the deformed geometry and effective plastic strains of the CGPed 304 ASS samples after first and second passes, respectively. The FE analysis shows that CGPed processed 304 ASS resulted in a nearly uniform distribution (see Fig. 3d) of strain. In every stage of the first and second passes of CGP, some inhomogeneity in strain was observed across the specimen as shown in Fig. 4, the same was also reported by Yoon et al. (Ref 25) and Niranjan et al. (Ref 26). In both passes, a wavy strain distribution is observed. During CGP (both passes 1 and 2), the same behavior is observed showing higher amplitudes of strain in case of flattening with respect to grooving. This deviation in strain during any pass becomes more uniform (less deviation) after completion of that pass. Distributions of the strain encountered in the specimen in different stages of the two passes of the CGP are presented in Fig. 5 which is in good agreement with the analytical results as compared in Fig. 6. The first grooving results in a strain magnitude of 0.58 as per calculation (according to Eq. 1); however, by FE analysis, the strain magnitude achieved 0.526 only in the first flattening stage. Subsequent processing steps/stages achieve greater harmony between analysis and FEM: after one complete pass, the analytical strain is 1.16, whereas FEM gives 1.15. Likewise,
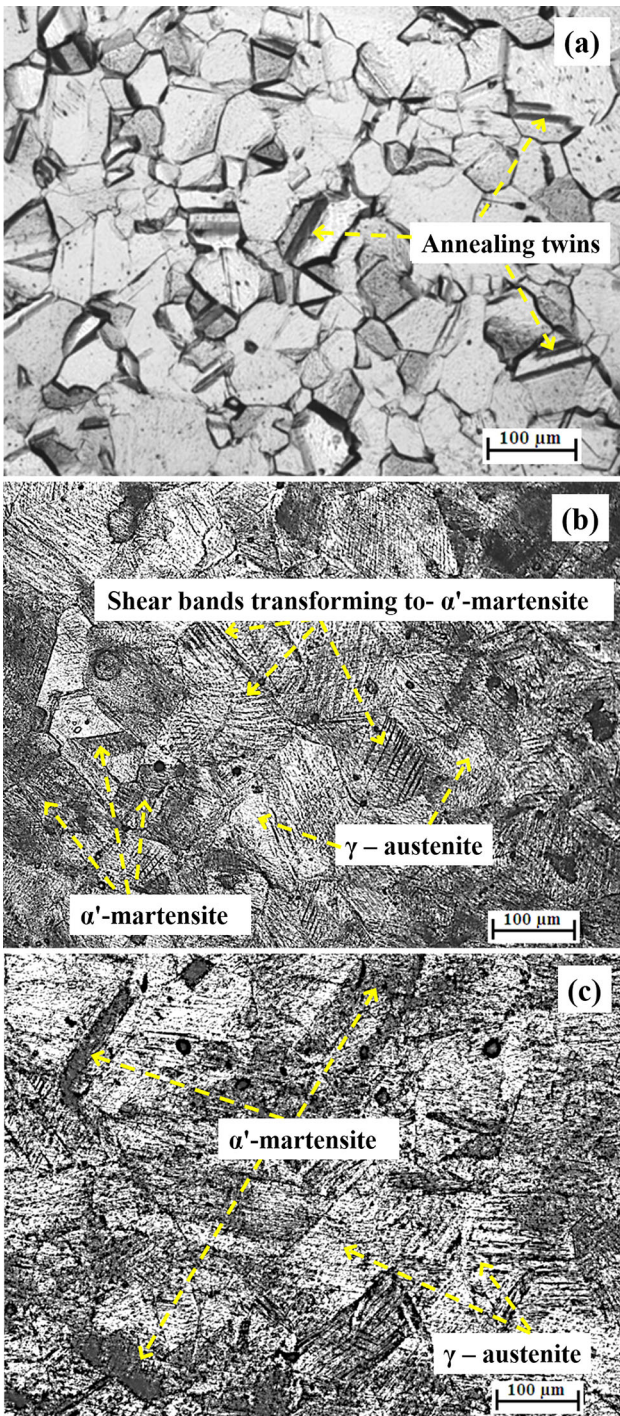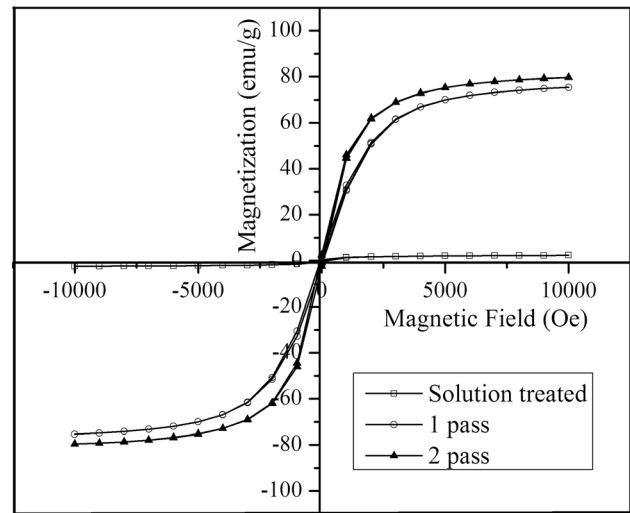
Fig. 9 Light optical micrographs of solution-treated (a), one pass (b), and two passes CGPed 304 ASS samples (c)

Fig. 10 Magnetization plot against the magnetic field for CGPed and solution-treated 304 ASS

the deviation between analysis and FEM is negligible also at the end of the second pass where the analytical strain value is 2.32, whereas FEM gives 2.29.

3.2 Microstructural Analysis

3.2.1 XRD Analysis. XRD patterns of the solution-treated and CGP-processed 304 ASS specimens after one and two passes are shown in Fig. 7. Reflections from the planes (111), (200), (220) and (311) can be observed for austenitic

phase (γ) in solution-treated condition. New diffraction peaks of α'-phase (deformation-induced martensite) emerge diminishing the peaks of existing γ-phase (austenite) during CGP. This clearly indicates the evolution of martensitic phase in 304 ASS during CGP. Martensitic peaks indexed with reflections (110), (200) and (211) clearly indicate the increase in martensitic phase with the number of CGP passes. Thin dotted lines (Red color) headed with upward arrow show emergence of α'-phase, and thick dotted line (Blue color) headed downward shows disappearance of γ-phase.

Figure 8 depicts an example of a Rietveld plot of the 304ASS after the second pass. The crystallographic planes in XRD spectra were identified and indexed in accordance with the α' and γ-phase. The refinement is shown as continuous line, whereas the experimental data are shown with points. From the Rietveld refinement, lattice microstrain and crystallite size were evaluated for the solution-treated and CGPed specimens. Lattice microstrain from Rietveld analysis was used to estimate the average internal dislocation density (ρ_{int}) using Eq. 3 (Ref 27).

$$\rho_{\text{int}} = \sqrt{\frac{3nk}{F}} \frac{e_{\text{RMS}}}{b \cdot D_{\text{eff}}} \qquad \text{(Eq 3)}$$

where, b is Burger's vector, e_{RMS} is root mean square lattice microstrain, D_{eff} is crystallite size, n and F are constants, and k is constant with values 14.4 for BCC and 16.1 for FCC crystal structure. The dislocation density was calculated with $n = F = 1$ and $b = 2.50 \times 10^{-10}$ and 2.87×10^{-10} m for BCC and FCC crystal structure, respectively (Ref 27). Lattice microstrain was estimated using Popa model (Ref 28) through Rietveld refinement. R_w and R_{wnb} (no background) values of Rietveld refinement were found to be smaller than 10% in all the refinements. Values obtained for crystallite size, lattice microstrain and average internal dislocation density for solution-treated and CGP processed samples with R_w and R_{wnb} values are tabulated in Table 1. It can be observed that in solution-treated condition, the value of microstrain is minimum, while crystallite size is maximum. As the steel is processed, the crystallite size of both phases (α' and γ- phases) decreases with increment in microstrain values. Dislocation densities were

Table 2 The volume % of martensite and austenite in the solution-treated and CGPed 304 ASS specimens obtained via XRD (using MAUD) and VSM analysis

State of Material	Through XRD analysis		Through VSM analysis	
	α′-Martensite, %	γ- Austenite, %	α′-Martensite, %	γ-Austenite, %
Solution treated	1.51	98.49	1.20	99.80
1 Pass CGPed	53.94	46.06	48.97	51.03
2 Pass CGPed	62.17	37.81	51.73	48.24

found to be increased for both the phases in the specimens with each CGP pass. Roy et al. (Ref 29) also reported the reduction in crystallite size of austenitic and martensitic phases with the increase in microstrain and dislocation density.

Naghizedah and Mirzade (Ref 30) have reported the dislocation density 1×10^{15} m^{-2} and 10×10^{15} m^{-2} for as-received and 75% cold rolled austenitic stainless steel, respectively. The difference in crystallite size and microstrain in both aforementioned conditions, as well as in the present work, is due to the difference in chemical composition of these alloys and their processing route. The deformation-induced strain in the material influences the mechanical properties in several ways. Dislocations play a vital role in governing mechanical properties because plastic deformation heavily depends on dislocations motion. Strengthening mechanisms are based on the principle of impeding the motion of dislocations. Obstructing the movement of dislocations makes the material stronger and harder. During CGP, work hardening takes place which results in an increase in dislocation density and decrease in crystallite size because of the generation and accumulation of dislocations. This is also confirmed by Rietveld analysis of XRD patterns as shown in Table 1. Furthermore, XRD profiles also indicate the formation of hard martensite phase during the course of CGP deformation (see Fig. 1).

3.2.2 Evolution of Martensite During CGP of 304 ASS. As discussed in the previous section, the deformation-induced martensite α′ is formed due to the excessive plastic straining during CGP. The nucleation sites for the martensite formation can be deformation twins, stacking faults and ε-martensite (Ref 31). Stacking fault energy (SFE) of alloys plays a key role in controlling the peculiarities of the mechanism for martensitic transformation. Two major paths for the generation of martensite in ASS can be identified based on their stacking fault energies (SFE) (Ref 32, 33).

(1) γ-austenite → ε-martensite → α′-martensite (SFE < 18 mJ/m^2), and

(2) γ-austenite → twinned austenite → α′-martensite (SFE > 18 mJ/m^2).

The empirical equation for calculation of SFE employing the elemental % composition (Ref 34) is as:

$$SFE\ (mJ/m^2) = -53 + 6.2(\%Ni) + 0.7(\%Cr)$$
$$+ 3.2(\%Mn) + 9.3(\%Mo) \qquad (Eq\ 4)$$

Incorporating the chemical composition of 304 ASS in Eq. 4, SFE of 304 ASS is estimated to be 19 mJ/m^2. Based on this SFE analysis, it can be proposed that twinned austenite transforms to α′-martensite. Solution-treated 304 ASS consists of twinned austenite that further transforms to intersecting

micro-shear bands during CGP. Furthermore, under the ongoing deformation, these shear bands act as nucleation sites for α′-martensite. Figure 9(a) depicts the light optical micrograph of solution-treated 304 ASS, and annealing twins are marked with the arrows. Figure 9(b) depicts the transformed martensite, shear band transforming to α′-martensite and remaining untransformed parent austenite after the first pass of CGP (Ref 31). With further CGP processing after pass 2 as depicted in Fig. 9(c), volume fraction of α′-martensite increases that resembles as the dark etched regions.

3.2.3 Characterization of Substructure Employing VSM and EBSD. As discussed in Sect. 3.2.1, CGPed 304 ASS has both austenite and martensite phases. The martensite phase has evolved during processing. The crystal structures as well as magnetic characteristics of martensite and austenite differ. The austenitic phase is paramagnetic at ambient condition, i.e., it shows nearly zero saturation magnetization. In contrast, martensitic phase is ferromagnetic (Ref 35) and responds to the magnetic field. The amount of conversion of austenite to martensite phase as a result of deformation is dependent on the amount of strain developed during processing. The amount of martensitic transformation can be identified using magnetization curves. Figure 10 shows magnetization plots of 304 ASS which confirms the presence of martensite phase after CGP. It is observed that, with the increase in number of passes there is an increase in the values of saturation magnetization.

The amount of saturation magnetization is less after the first pass (75 emu/g) than after second pass (79 emu/g). It shows the increase in the ferromagnetic characteristics in the specimens with CGP. The same behavior, i.e., with the increase in the amount of straining in 304 ASS, there is an increase in volume percent of deformation-induced martensite (Ref 4, 36). The volume percentage of austenite and martensite phases after analyzing the VSM and XRD data is tabulated in Table 2 for CGPed and solution-treated specimens. It is observed from Table 2 that there is a difference in the volume percentage of martensite and austenite phases estimated from the two aforementioned techniques. This difference in estimates is attributed to the fact that x-ray penetrates only up to few micrometers; thus, it gives information close to the surface of deformed specimens. However, the VSM provides the volumetric information of the whole sample.

To understand the evolution of substructure during CGP, EBSD measurements were also performed. Typical microstructures of solution-treated and deformed specimens developed during different passes (pass 1 and pass 2) of CGP of 304 ASS obtained after EBSD measurements in form of Inverse Pole Figure (IPF) maps are shown in Fig. 11(a, c and e). Figure 11(a) shows the IPF map for solution-treated specimen which indicates the presence of coarse grain structure. During
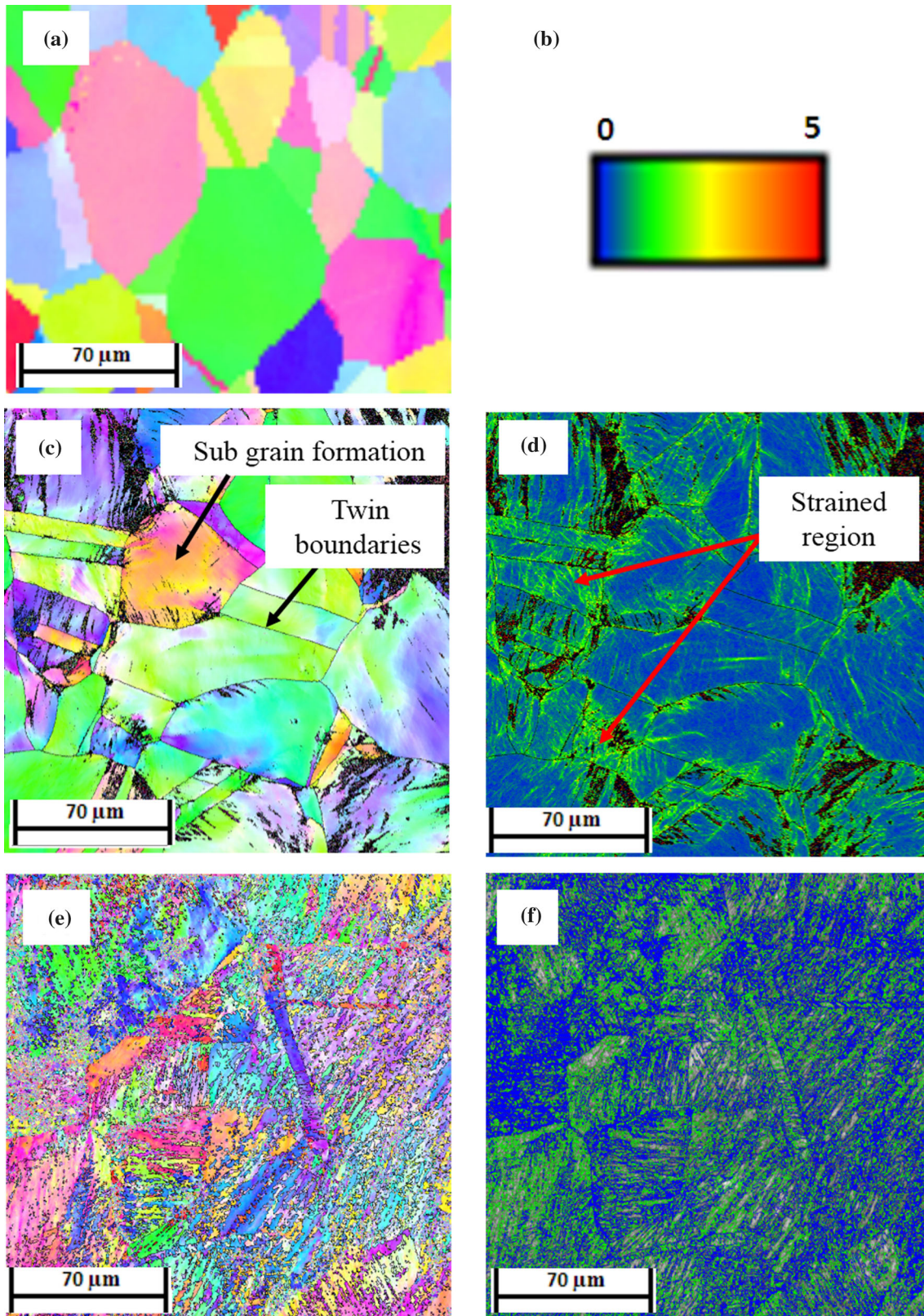
Fig. 11 IPF map of the solution-treated specimen (a), the legend of KAM maps (b), IPF map of CGPed specimen after pass 1 (c) and pass 2 (e); and KAM maps of CGPed specimen after pass 1 (d) and pass 2 (f). Different colors in IPF maps represent randomly oriented grains
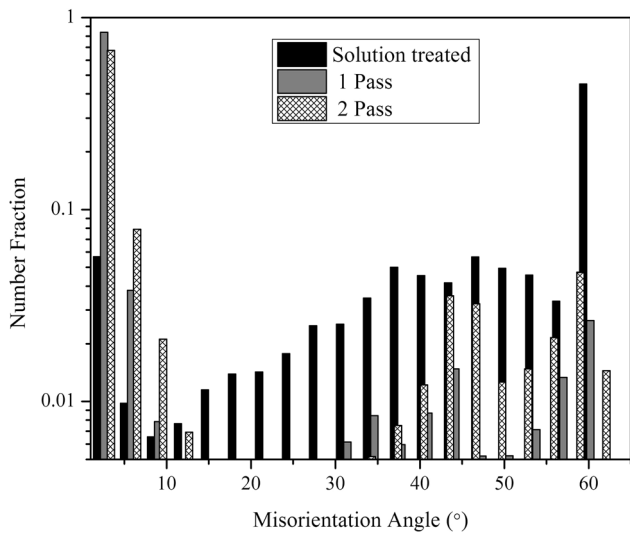
Fig. 12 Histograms of misorientation angle of solution-treated and CGPed specimens

CGP, substructure formation takes place and subgrains are developed within the grains. Figure 11(c) shows the formation of subgrains (marked with arrow) represented by the gradient of color within grains as well as the presence of twin boundaries. Figure 11(d and f) represents the Kernel Average Misorientation (KAM) maps of CGP-processed 304 ASS, and legends of KAM maps are depicted in Fig. 11(b). In KAM maps, the green area represents hardened region as a result of deformation-induced martensitic transformation. The amount of martensitic transformation increases with further processing as seen in Fig. 11(f), i.e., after the second pass of CGP. Figure 12 depicts the distribution of misorientation angle obtained from EBSD in the solution-treated and CGPed samples. The value of KAM is higher for 2 pass (1.78), in comparison with 1 pass (0.75).

In solution-treated specimen, a large amount of high angle grain boundaries (HAGBs) is observed and the fraction of twin boundaries having misorientation 60º is 0.60. As the specimens undergo CGP, plastic deformation influences the development of substructures and more subgrain boundaries are formed. The extent of subgrain formation is a little high for the pass 2 specimen which is reflected as the increase in number fraction
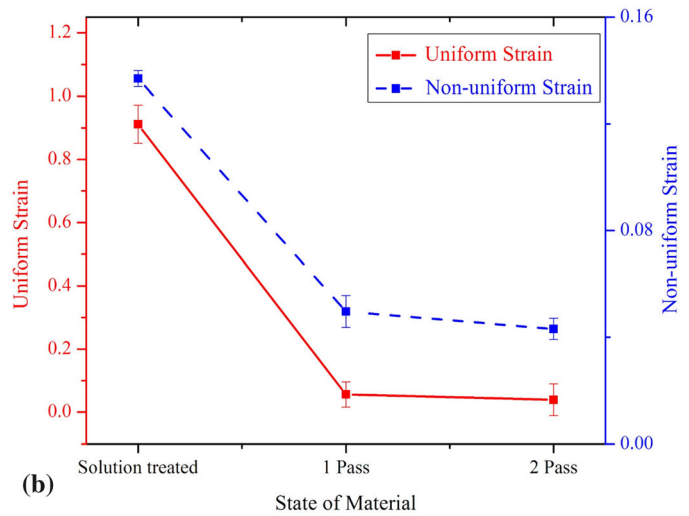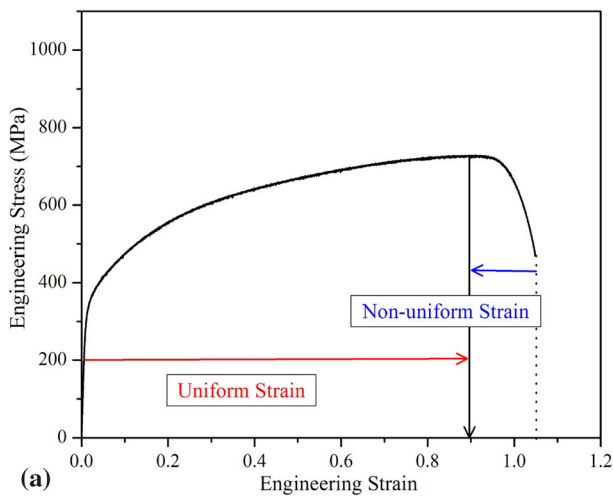
Fig. 13 Uniform and non-uniform strain in the stress–strain plot of solution-treated 304 ASS (a) and influence of CGP passes on the uniform and non-uniform strain (b)
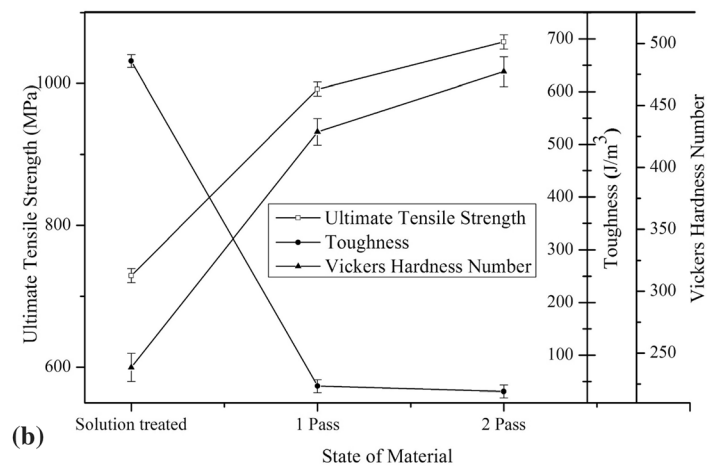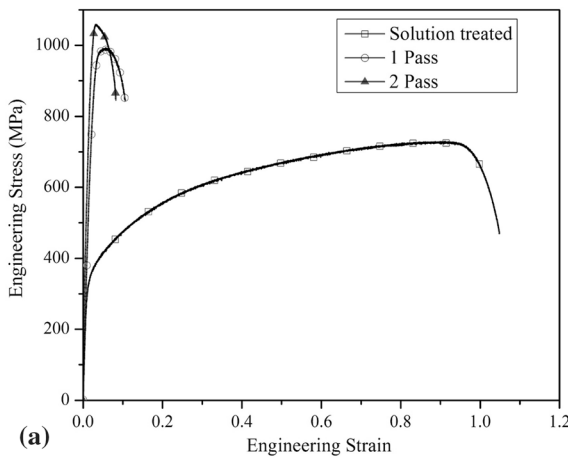
Fig. 14 Effect of CGP processing over 304 ASS mechanical properties: Stress–strain plots of solution-treated and CGP processed specimens (a) and variation in ultimate tensile strength, toughness, and Vicker's hardness with CGP passes (b)

Table 3 Mechanical behavior of Type 304 steel processed through different routes

S. No	Processing route	Material	Processing condition	Initial 304 steel properties			Processed 304 steel properties			References
				Yield strength, MPa	UTS, MPa	Hardness, VHN	Yield strength, MPa	UTS, MPa	Hardness, VHN	
1	RTR	304	30%	258	579	188	926	1000	336	(Ref 1)
2	RTR	304	30%	...	693	208	...	922	350	(Ref 5)
3	ECAP	304	3 Pass	...	...	200	...	...	470	(Ref 39)
4	Asymmetric cold rolling	304	30%	207	662	220	964	1019	448	(Ref 40)
5	CGP	304	2 Pass	...	729	238	...	1058	477	Present study

RTR room temperature rolling, *ECAP* equal channel angular pressing

of low angle grain boundaries (LAGBs) having misorientation less than 10°. This substructure formation in terms of subgrain boundaries indicates the increase in the number of geometrically necessary dislocations that shall lead to further strengthening of CGP processed materials.

3.3 Influence of CGP on Mechanical Properties

Figure 13(a) shows the tensile behavior of solution-treated 304 ASS, which illustrates the regions of uniform and non-uniform strains. It can be visualized that the area under uniform strain is higher in comparison with non-uniform strain. Figure 13(b) shows the variation in uniform and non-uniform strain with CGP, and it is found that both values decrease with CGP. Figure 14 depicts the effect of CGP processing on mechanical properties of 304 ASS. Figure 14(a) shows engineering stress–strain curves of 304 ASS solution-treated and after CGP. The variation of UTS values with respect to the number of passes is shown in Fig. 14(b). Results show that the improvement in UTS during the CGP process after the first pass is higher than after the second pass. CGP processing increases UTS of solution-treated 304 ASS from 729 to 992 MPa after the first pass, representing a rise of approximately 36%. The second pass induces a rise of merely 6% in UTS is noticed with respect to first pass and UTS thus achieves 1058 MPa, representing a gross increase of 44% after second pass with respect to solution-treated sample. Increased microstrain, smaller crystallite size and higher average dislocation density resulting from the CGP are the paramount factors for enhancement in mechanical properties (Ref 37, 38). The other factor responsible for enhancement in UTS is the evolution of strain-induced martensite phase during CGP. Additionally, a significant decrease in ductility and toughness is noticed which is attributed to material hardening during the course of CGP.

Figure 14(b) also shows the hardness of the solution-treated and samples processed by CGP technique up to two passes. The hardness values increase with the number of CGP passes. Same as for UTS, the increment in hardness values is quite prominent in first pass (Ref 5). The hardness values have increased from 238 to 477 VHN (gross increase 100%) after completion of two passes of CGP. The increase in hardness value can be attributed to the formation of deformation-induced martensite (α'-phase), increased dislocation density and decreased crystallite size. The effect of CGP process is compared with other processing techniques, and the comparative study is tabulated in Table 3.

The results obtained from present study show good combination of strength and hardness.

4. Conclusions

In the present work, 304 was successfully processed through CGP. The work provides deep insight over the microstructural development and its correlation with mechanical properties through XRD, VSM, EBSD and LOM. The major findings of the present study are outlined below:

- FE analysis of CGP process for 304 ASS shows an effective strain of 2.29 after the two passes which is in good agreement with analytical results, i.e., 2.32.
- The ultimate tensile strength of 304 ASS increases from 729 to 1058 MPa after successful completion of two passes of CGP. Similarly, the hardness values increased from 238 to 477 VHN after completion of two passes of CGP. This improvement in ultimate tensile strength and hardness is 44% and 100% in comparison with solution-treated sample, respectively.
- Both, ductility and toughness decrease significantly with the increase in the number of CGP passes.
- The improvement in UTS and hardness is the synergistic effect of different variables such as, increased average dislocation density and microstrain of both phases, reduced crystallite size of both phases, substructure formation and the formation of deformation-induced martensite.
- The significant improvement, in terms of mechanical properties, took place during the first pass of the processing, and thus, it can be proposed that one pass of CGP is adequate for the improvement in mechanical properties from the economic point of view, which makes CGP an effective technique to improve mechanical properties.

References

1. M. Milad, N. Zreiba, F. Elhalouani, and C. Baradai, The effect of cold work on structure and properties of AISI, 304 stainless steel, *J. Mater. Process. Technol.*, 2008, **203**, p 80–85

2. A. Hedayati, A. Najafizadeh, A. Kermanpur, and F. Forouzan, The effect of cold rolling regime on microstructure and mechanical properties of AISI, 304L stainless steel, *J. Mater. Process. Technol.*, 2010, **210**, p 1017–1022

3. G.S. Sun, L.X. Du, J. Hu, H. Xie, H.Y. Wu, and R.D.K. Misra, Ultrahigh strength nano/ultrafine-grained 304 stainless steel through three-stage cold rolling and annealing treatment, *Mater. Char.*, 2015, **110**, p 228–235

4. R. Singh, S. Goel, R. Verma, R. Jayaganthan, and A. Kumar, Mechanical behavior of 304 austenitic stainless steel processed by room temperature rolling, *IOP Conf. Ser. Mater. Sci. Eng.*, 2017, **330**, p 012017

5. A.K. Gupta, T.S. Maddukuri, and S.K. Singh, Constrained groove pressing for sheet metal processing, *Prog. Mater Sci.*, 2016, **84**, p 403–462

6. D.H. Shin, J.J. Park, Y.S. Kim, and K.T. Park, Constrained groove pressing and its application to grain refinement of aluminum, *Mater. Sci. Eng. A*, 2002, **328**, p 98–103

7. A. Krishnaiah, U. Chakkingal, and P. Venugopal, Production of ultrafine grain sizes in aluminium sheets by severe plastic deformation using the technique of groove pressing, *Scr. Mater.*, 2005, **52**, p 1229–1233

8. J. Zrnik, T. Kovarik, Z. Novy, and M. Cieslar, Ultrafine-grained structure development and deformation behavior of aluminium processed by constrained groove pressing, *Mater. Sci. Eng. A*, 2009, **503**, p 126–129

9. M. Shantharaja, Mechanical behaviour of pure aluminum processed by constrained groove pressing, *J. Mater. Sci. Eng.*, 2013, **2**, p 1–5

10. F. Khakbaz and M. Kazeminezhad, Work hardening and mechanical properties of severely deformed AA3003 by constrained groove pressing, *J. Manuf. Process.*, 2012, **14**, p 20–25

11. F. Nazari, M. Honarpisheh, and H. Zhao, Effect of stress relief annealing on microstructure, mechanical properties, and residual stress of a copper sheet in the constrained groove pressing process, *Int. J. Adv. Manuf. Technol.*, 2019, **102**, p 4361–4370

12. S.S.S. Kumar and T. Raghu, Mechanical behaviour and microstructural evolution of constrained groove pressed nickel sheets, *J. Mater. Process. Technol.*, 2013, **213**, p 214–220

13. M. Moradpour, F. Khodabakhshi, S.R. Mohebpour, H. Eskandari, and M. Haghshenas, Finite element modeling and experimental validation of CGP classical and new cross routes for severe plastic deformation of an Al-Mg alloy, *J. Manuf. Process.*, 2019, **37**, p 348–361

14. M. Ebrahimi, Sh Attarilar, F. Djavanroodi, C. Gode, and H.S. Kim, Wear properties of brass samples subjected to constrained groove pressing process, *Mater. Des.*, 2014, **63**, p 531–537

15. X. Mou, K. Peng, J. Zeng, L.L. Shaw, and K.W. Qian, The influence of the equivalent strain on the microstructure and hardness of H62 brass subjected to multi-cycle constrained groove pressing, *J. Mater. Process. Technol.*, 2011, **211**, p 590–596

16. F. Khodabakhshi, M. Kazeminezhad, and A.H. Kokabi, Constrained groove pressing of low carbon steel: nano-structure and mechanical properties, *Mater. Sci. Eng. A*, 2010, **527**, p 4043–4049

17. S. Kumar, K. Harihan, R.K. Digavalli, and S.K. Paul, Accounting Bauschinger effect in the numerical simulation of constrained groove pressing process, *J. Manuf. Process*, 2019, **38**, p 49–62

18. I. Karademir, M.B. Celik, F. Husem, E. Maleki, A. Amanov, and O. Unal, Effects of constrained groove pressing, severe shot peening and ultrasonic nanocrystal surface modification on microstructure and mechanical behavior of S500MC high strength low alloy automotive steel, *Appl. Surf. Sci.*, 2021, **538**, p 147935

19. S. Shahraki, H. Miyanji, and H. Abdollahi, Microstructure and mechanical properties of ultrafine-grained IF steel sheets produced by constrained groove pressing, *Eng. Solid Mech.*, 2020, **8**, p 63–68

20. K.S. Fong, D. Atsushi, T.M. Jen, and B.W. Chau, Effect of deformation and temperature paths in severe plastic deformation using groove pressing on microstructure, texture, and mechanical properties of AZ31-O, *J. Manuf. Sci. Eng.*, 2015, **137**, p 1–16

21. F. Nazari and M. Honarpisheh, Analytical and experimental investigation of deformation in constrained groove pressing process, *J. Mech. Eng. Sci.*, 2018, **233**(11), p 3751–3759

22. F. Khodabakhshi, M. Abbaszadeh, S.R. Mohebpour, and H. Eskandari, 3D finite element analysis and experimental validation of constrained groove pressing–cross route as an SPD process for sheet form metals, *Int. J. Adv. Manuf. Technol.*, 2014, **73**, p 1291–1305

23. M. Ebrahimi and F. Djavanroodi, Experimental and numerical analyses of pure copper during ECFE process as a novel severe plastic deformation method, *Prog. Nat. Sci.: Mater. Int.*, 2014, **24**, p 68–74

24. B.H. Toby, R factor in Rietveld analysis: how good is good enough?, *Powder Diffrac.*, 2006, **21**, p 67–70

25. S.C. Yoon, A. Krishnaiah, U. Chakkingal, and H.S. Kim, Severe plastic deformation and strain localization in groove pressing, *Compu. Mater. Sci.*, 2008, **43**, p 641–645

26. G.G. Niranjan and U. Chakkingal, Deep draw ability of commercial purity aluminum sheets processed by groove pressing, *J. Mater. Process. Technol.*, 2010, **210**, p 1511–1516

27. S.D. Yadav, M.E. Tahawy, S. Kalacska, M. Domankova, D.C. Yubero, and C. Poletti, Characterizing dislocation configurations and their evolution during creep of a new 12% Cr steel, *Mater. Char.*, 2017, **134**, p 387–397

28. N.C. Popa, The (hkl) dependence of the diffraction-line broadening caused by strain and size for all laue groups in rietveld refinement, *J. Appl. Crystall.*, 1998, **31**, p 176–180

29. B. Roy, R. Kumar, and J. Das, Effect of cryorolling on the microstructure and tensile properties of bulk nano-austenitic stainless steel, *Mater. Sci. Eng. A*, 2015, **631**, p 241–247

30. M. Naghizadeh and H. Mirzade, Processing of fine grained AISI, 304L austenitic stainless steel by cold rolling and high-temperature short-term annealing, *Mater. Res. Exp.*, 2018, **5**, p 056529

31. M. Hadji and R. Badji, Microstructure and mechanical properties of austenitic stainless steels after cold rolling, *J. Mate. Eng. Perform.*, 2002, **11**, p 145–151

32. G.B. Olsen and M. Cohen, Kinetics of strain induced martensitic nucleation, *Metall. Trans. A*, 1975, **6**, p 791–795

33. K. Sato, M. Ichinose, Y. Ohirotsu, and Y. Inoue, Effect of deformation induced phase transformation and twinning on mechanical properties of austenitic Fe-Mn-Al alloy, *ISIJ Int.*, 1989, **29**, p 868–877

34. R.E. Schramm and R.P. Reed, Stacking fault energies of seven commercial austenitic stainless steels, *Metall. Trans. A*, 1975, **6**, p 1345–1351

35. K. Mumtaz, S. Takahashi, J. Echigoya, Y. Kamada, L.F. Zhang, H. Kikuchi, K. Ara, and M. Sato, Magnetic measurements of martensitic transformation in austenitic stainless steel after room temperature rolling, *J. Mater. Sci.*, 2004, **39**, p 85–97

36. R. Singh, D. Sachan, S. Goel, R. Verma, R. Jayaganthan, A. Kumar, Mechanical behavior of 304 austenitic stainless steel processed by cryogenic rolling, *Mater. Today: Proc.*, 2018, **5**, p 16880–16886

37. R. Singh, G. Rajan, B.K. Kumar, R. Verma, D. Singh, P.N. Rao, and A. Kumar, Numerical analysis of constrained groove pressing and mechanical behavior of processed 316L stainless steel, *Mater. Sci. Forum*, 2019, **969**, p 901–908

38. V. Shankar, S.D. Yadav, and K. Mariappan, Influence of W and effect of loading mode on the substructural evolution of reduced activation ferritic/martensitic (RAFM) steels, *Mater. Lett.*, 2019, **234**, p 257–260

39. M. Tofaninejad and M.N. Ahmadabadi, Effect of equal channel angular pressing on the microstructure and mechanical properties of AISI, type 304 austenitic stainless steel, *Open J. Adv. Mater. Res.*, 2014, **829**, p 86–90.A

40. R. Amininejad and J. Jamaati, Hosseinipour, achieving superior strength and high ductility in AISI, 304 austenitic stainless steel via asymmetric cold rolling, *Mater. Sci. Eng. A*, 2019, **767**, p 138433